Nano Research 2017, 10(7): 2193–2209
DOI 10.1007/s12274-017-1453-2
Research Article
ISSN 1998-0124
CN 11-5974/O4

Enhanced photocatalytic activity by the construction of a TiO_2/carbon nitride nanosheets heterostructure with high surface area via direct interfacial assembly

Zili Xu[1,§], Chuansheng Zhuang[2,§], Zhijuan Zou[1], Jingyu Wang[1] (✉), Xiaochan Xu[1], and Tianyou Peng[2] (✉)

[1] *Key Laboratory of Material Chemistry for Energy Conversion and Storage (Ministry of Education), School of Chemistry and Chemical Engineering, Huazhong University of Science and Technology, Wuhan 430074, China*
[2] *College of Chemistry and Molecular Sciences, Wuhan University, Wuhan 430072, China*
[§] *These authors contributed equally to this work.*

Received: 3 November 2016
Revised: 27 December 2016
Accepted: 1 January 2017

KEYWORDS
carbon nitride nanosheets,
TiO_2,
hybrid photocatalyst,
interfacial assembly,
high surface area

ABSTRACT

A TiO_2 heterostructure modified with carbon nitride nanosheets (CN-NSs) has been synthesized via a direct interfacial assembly strategy. The CN-NSs, which have a unique two-dimensional structure, were favorable for supporting TiO_2 nanoparticles (NPs). The uniform dispersion of TiO_2 NPs on the surface of the CN-NSs creates sufficient interfacial contact at their nanojunctions, as was confirmed by electron microscopy analyses. In comparison with other reported metal oxide/CN composites, the strong interactions of the ultrathin CN-NSs layers with the TiO_2 nanoparticles restrain their re-stacking, which results in a large specific surface area of 234.0 $m^2 \cdot g^{-1}$. The results indicate that the optimized TiO_2/CN-NSs hybrid exhibits remarkably enhanced photocatalytic efficiency for dye degradation (with k of 0.167 min^{-1} under full spectrum) and H_2 production (with apparent quantum yield = 38.4% for λ = 400 ± 15 nm monochromatic light). This can be ascribed to the improved surface area and quantum efficiency of the hybrid, with a controlled ratio that reaches the appropriate balance between producing sufficient nanojunctions and absorbing enough photons. Furthermore, based on the identification of the main active species for photodegradation, and the confirmation of active sites for H_2 evolution, the charge transfer pathway across the TiO_2/CN-NSs interface under simulated solar light is proposed.

1 Introduction

Due to the growing energy and environmental crisis, much attention has been focused on exploring highly efficient photocatalysts that can promote the direct use of abundant solar energy resources to drive reactions. As a typical inorganic semiconductor photocatalyst, TiO_2 has been widely investigated in the fields of

Address correspondence to Jingyu wang, jingyu.wang@163.com; Tianyou Peng, typeng@whu.edu.cn

sunlight-driven pollutant decomposition and energy conversion because of its strong oxidizing power, high thermal/chemical/photo- stability, low cost, non-toxicity, etc. However, it suffers from a limited solar light absorption, and low quantum efficiency [1, 2]. The coupling of photocatalysts with narrow bandgap semiconductors is considered to be a competitive strategy to extend its light response into the visible range, and reduce the charge recombination losses [3, 4]. Graphitic carbon nitride (CN) has been recently identified as a superior candidate for this owing to its visible light driven bandgap (~2.7 eV), and suitable band-edge positions matching with those of TiO_2. There are many reports regarding TiO_2/CN hetero-structures constructed by hydrothermal, calcination, and impregnation strategies [5–9]. For instance, the CN-hybridized TiO_2 obtained in our previous work exhibited an enhanced photocatalytic performance under UV and visible light, as a result of charge carriers efficiently transferring at the heterojunction interface, and CN sensitization for visible light harvesting [10].

It should be noted that CN in composites is usually a bulk material with an extremely low specific surface area (e.g. 3.7 $m^2 \cdot g^{-1}$ from melamine, and 9.2 $m^2 \cdot g^{-1}$ from dicyandiamide), and less active sites; therefore, its photocatalytic activity is significantly restricted [11–13]. When constructing heterostructures, the low surface area of bulk CN does not allow for enough contact to occur with the TiO_2 crystals for efficient charge carrier transport. Hao et al. reported that the surface area of g-C_3N_4/TiO_2 was increased to 70.2 $m^2 \cdot g^{-1}$ when a macro/mesoporous structure was fabricated [5]. Jiang et al. designed TiO_2 yolk–shell spheres coupled with bulk CN to improve its specific surface area. The optimized catalyst (TCN-2.0), however, possessed a surface area of 93 $m^2 \cdot g^{-1}$, even though the pure TiO_2 spheres had a surface area as high as 157 $m^2 \cdot g^{-1}$ [6]. In addition, weak van der Waals interactions between the layers slowed down the electron transfer, which led to a high recombination rate of photogenerated electron (e^-)–hole (h^+) pairs, and the low electrical conductivity of bulk CN materials [14].

As an analogue of graphite, the CN polymer possesses a stacked two-dimensional (2D) structure that can be exfoliated into 2D nanosheets (CN-NSs) of few atomic layers [15–18]. Similar to graphene oxide, the liquid-phase exfoliation process improves the specific surface area and water-dispersibility of CN catalysts, making them a promising substrate-support for nanoparticles (NPs) [19]. In addition, owing to the notable merits of 2D π-conjugated materials, the graphene-analogue structure gives rise to an increased conductivity and charge carriers transport [17, 18].

At present, few reports have dwell on the construction of TiO_2 crystals on CN-NSs. Most recently, Han et al. synthesized graphitic CN-NSs hybridized N-doped TiO_2 nanofibers (GCN/NT NFs) via an electrospinning process, combined with a modified heat-etching method. The hybrid, with an increased surface area of 47.3 $m^2 \cdot g^{-1}$ and under simulated solar light, presented a highly efficient photocatalytic H_2 production rate and degradation activity [20]. Li et al. reported a seed-induced solvothermal approach to grow TiO_2 nanostructures on g-C_3N_4 nanosheets. The hybrid, with an optimum surface area of 102 $m^2 \cdot g^{-1}$, exhibited enhanced photocatalytic activity towards methyl orange and phenol degradation under visible light [21]. Tong et al. developed a biomimetic method for fabricating g-C_3N_4/TiO_2 nanosheets with an enlarged surface area (109 $m^2 \cdot g^{-1}$) and enhanced photocatalytic activity toward the degradation of organic pollutants [22]. In actuality, it has been reported that the surface area can be much higher when the supporting metal oxide crystals are placed on other 2D materials, for example MoS_2 and graphene, which had surface areas of 186 and 199.8 $m^2 \cdot g^{-1}$, respectively [23, 24].

Although the liquid-phase exfoliation method successfully yields ultrathin CN-NSs of few atomic layers, the isolated CN layers can only maintain their original morphology in aqueous solutions. When the hydrosol is dried into the powders needed for the heterogeneous photocatalysis, the isolated layers are inclined to re-stack into a bulk structure, and therefore a dramatic decrease in the specific surface area is observed [17]. In the present study, we developed a direct interfacial assembly strategy to construct well-contacted 0D/2D TiO_2/CN-NSs heterostructures. The sheet-like morphology of the CN-NSs was partly preserved in the composite powders, presumably due to the uniform dispersion of the nano-sized TiO_2 NPs on their surface. This intimate contact between them hinders the re-stacking of the exfoliated CN-NSs layers.

To the best of our knowledge, among the reported metal oxide/CN composites, the TiO_2/CN-NSs hybrid reported here, with a controlled ratio, possesses the highest specific surface area, with a value of 234.0 $m^2 \cdot g^{-1}$. The optimized hybrid behaves as a highly efficient photocatalyst towards dye degradation and H_2 production under simulated solar light. Furthermore, the synergetic effect between TiO_2 and the CN-NSs was investigated in detail. This work provides a facile route for constructing semiconductor/CN-NSs heterostructures for their potential use in solar energy driven reactions.

2 Experimental

2.1 Synthetic procedure

Bulk CN was prepared by directly heating dicyandiamide to 550 ℃ in a muffle furnace, and at a heating rate of 15 ℃·min^{-1}. This temperature was maintained for 4 h. The ultrathin CN-NSs were obtained by a liquid-phase exfoliation method. First, 300 mg of bulk CN powder were dispersed in 30 mL of concentrated sulfuric acid, under stirring, for 12 h. The resulted aqueous suspension was diluted to 100 mL water, and then treated by ultrasonication for 2 h. Thereafter, the mixture was centrifuged and washed with water until its pH reached 7.0. The resulting precipitate was diluted to 30 mL water, and treated by ultrasonication for another 2 h. Lastly, the CN-NSs colloid was separated from the residual unexfoliated bulk materials by centrifugation. The mass concentration of the CN-NSs was calculated to be 1.0–1.2 mg·mL^{-1} from several repeated experiments.

The TiO_2 NPs were synthesized via a soft-chemical process based on the well-established method described in our previous work [25]. In brief, 3 mL of titanium tetra-n-butoxide were mixed with 22 mL of absolute ethanol, and then the solution was added dropwise into 30 mL of deionized water, under vigorous stirring. After this addition, the suspension was kept stirring at 70 ℃ for about 50 min to obtain a condensed solution. Subsequently, 70 mL of a 0.055 M HNO_3 aqueous solution were added, and the mixture was continuously stirred at 70 ℃ for 4 h under airproof conditions. Then, a 1.0 M NaOH solution was added to cause the sedimentation of the hydrosol. The precipitate was collected by centrifuging, washing, and re-dispersing into 100 mL of water with a mass concentration of TiO_2 NPs of 5.8–6.7 mg·mL^{-1}.

To achieve the uniform dispersion of the TiO_2 NPs on the CN-NSs, an interfacial assembly strategy was proposed here, as illustrated in Fig. 1. First, a stoichiometric weight ratio of TiO_2 and CN-NSs hydrosols were mixed and diluted to 30 mL with deionized water. The obtained colloids were sonicated for 3 h. This process was crucial for the formation of sufficient interfacial interaction between TiO_2 and the CN-NSs. Thereafter, the mixture was heated to 70 ℃ and stirred in a fume hood for 4 h. The solvent evaporation brought about the further assembly between the TiO_2 NPs and CN-NSs layers. Finally, the powder catalysts were collected by vacuum drying at 60 ℃ for 4 h, and milled into ultrafine powders. By

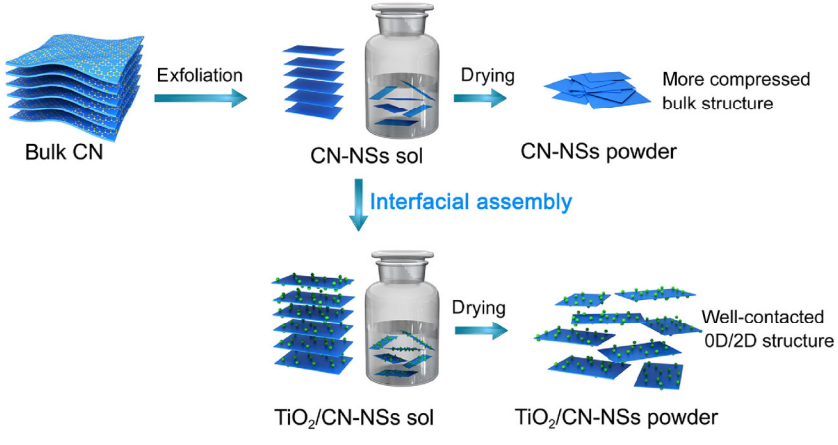

Figure 1 Schematic plot of the preparation of the TiO_2/CN-NSs heterostructure via the interfacial assembly strategy.

varying the mass proportion of TiO_2 to CN-NSs, a series of TiO_2/CN-NSs hybrids were synthesized, and labeled as TiO_2/CN-NSs (1:3), TiO_2/CN-NSs (1:1), TiO_2/CN-NSs (3:1), and TiO_2/CN-NSs (9:1). The TiO_2/CN-NSs hybrid that is frequently described in this work has the default ratio value of 3:1.

2.2 Characterization

Transmission electron microscopy (TEM) images were obtained using a Tecnai G2 F30 (FEI, Holland) apparatus. Atom force microscopy (AFM) images were obtained with a SPM9700 AFM. Fourier-transform infrared (FTIR) spectra were recorded on a Perkin Elmer spectrum 1000 with a KBr pellet. The X-ray powder diffraction (XRD) patterns were obtained with an X' Pert PRO instrument using a Cu Kα radiation source with λ_{Cu} = 0.15418 nm. The nitrogen adsorption and desorption isotherms were conducted at 77 K on a Micrometrics ASAP2000 system using the Brunauer–Emmett–Teller (BET) method. The chemical composition and binding energy of the samples were analyzed by X-ray photoelectron spectroscopy (XPS, AXIS-ULTRA DLD-600W). The binding energy (BE) shifts were corrected by setting the C 1s level to 285.0 eV, as an internal standard, to compensate for the surface-charging effect during the data acquisition. The thermogravimetric analyses (TGA) were performed on a Mettler Toledo TGA/SDTA851e at a heating rate of 10 ℃·min^{-1}, from room temperature to 800 ℃, under an air atmosphere. The UV–Vis diffuse reflectance spectra (DRS) of the samples were recorded on a Varian Cary 5E spectrophotometer. The photoluminescence (PL) spectra of the samples were measured on a fluorescence spectrometer (Hitachi F-7000).

2.3 Evaluation of the photocatalytic performance

The photocatalytic activities of the photocatalysts were measured by the degradation rate of rhodamine B (RB), and the evolution rate of H_2 under simulated solar light. A 300-W Xe lamp was used as the simulated solar light source. This lamp was positioned 25 cm away from the reactor. For the degradation tests, 5.0 mg of the photocatalyst were suspended in 10 mL of an aqueous solution containing 26 mg·L^{-1} of RB. Before irradiation, the suspensions were stirred for 40 min in the dark to establish an adsorption–desorption equilibrium. At scheduled irradiation time intervals, the suspension was sampled to measure any changes in the maximum absorption (c/c_0) of the RB absorption spectra. For the H_2 evolution test, the Pt loaded photocatalysts were prepared as follows. First, 0.1 g of the TiO_2/CN-NSs catalyst was suspended in a mixture consisting of 90 mL of distilled water and 10 mL of methanol, in a reaction cell, using a magnetic stirrer. Then, 0.5 wt.% Pt loaded TiO_2/CN-NSs photocatalysts were prepared by the standard photoreduction deposition method using a $H_2PtCl_6{\cdot}6H_2O$ aqueous solution. The photoreaction was performed in 100 mL of an aqueous suspension containing 50 mg of the catalyst, and 50 mM of ascorbic acid (AA) as a sacrificial reagent. The reactor was irradiated from the top after removing any residual air. The evolution of H_2 was analyzed with an online gas chromatographer (GC, SP6890, TCD detector, 5 Å molecular sieve columns, and Ar carrier). The apparent quantum yield (AQY) was calculated by Eq. (1) under monochromatic light irradiation obtained from the corresponding band-pass filter (for example, λ = 400 ± 15 nm).

$$\mathrm{AQY}(\%) = \frac{2 \times \text{number of evolved } H_2 \text{ molecules}}{\text{Number of incident photons}} \times 100\% \quad (1)$$

2.4 Electrochemical and photoelectrochemical measurements

The electrochemical impedance spectroscopy (EIS) and photocurrent were measured with a CHI650E electrochemical workstation (Chenhua Instruments, Shanghai, China) using a standard three-electrode system, which employed a platinum wire as the counter electrode, and a Ag/AgCl electrode as the reference electrode. First, 2 mg of sample powder were dispersed ultrasonically in 1 mL of water. Then, 75 μL of the resulting suspension was dip-coated on 10 mm × 10 mm piece of indium-tin oxide (ITO) glass electrode. After that, the electrode was dried in air at room temperature to eliminate any water, and heated to 60 ℃ to form a modified ITO electrode. The EIS was measured in a 0.1 M KCl solution containing 5 mM $Fe(CN)_6^{3-}/Fe(CN)_6^{4-}$ at the open circuit potential. A 0.1 M Na_2SO_4 solution was used as the electrolyte for the photocurrent measurements.

2.5 Trapping tests and detection of reactive oxygen species (ROS)

To investigate the synergetic effects between the TiO_2 and CN-NSs, trapping experiments were conducted to measure the contribution of the active species to the photocatalytic reaction. The scavengers used were 1 mM tert-butanol (t-BuOH) for $^{\cdot}OH$, 1 mM EDTA-2Na for h^+, and 0.3 mM benzoquinone (BQ) for $O_2^{-\cdot}$. The specified scavenger was added to the photocatalyst suspensions prior to the addition of the RB solution.

3 Results and discussion

3.1 Morphology and structure

The microscopic morphologies of the pristine CN, CN-NSs, TiO_2, and hybrid were investigated by TEM and AFM observations. As shown in Fig. 2(a), pristine bulk CN displayed a stacked layered structure at the micrometer scale. After exfoliation, the CN-NSs in the hydrosol presented a semi-transparent sheet-like morphology, suggesting an ultrathin thickness (Fig. 2(b)). As measured by AFM, the randomly selected NSs mostly possessed a planar size of several hundred nanometers, and a thickness of 1.4–2.3 nm, corresponding to 4–7 atomic layers (Figs. 2(c) and 2(d)). The pure TiO_2 hydrosol was composed of extremely small nanoparticles with a diameter of 4–8 nm (Fig. 2(e)). When introducing the CN-NSs, the ultrafine TiO_2 NPs were uniformly dispersed on the surface of the CN-NSs by interfacial assembly (Fig. 2(f)). The lattice fringe of the particles supported on the surface of the CN-NSs was measured to be 0.35 nm, and assigned

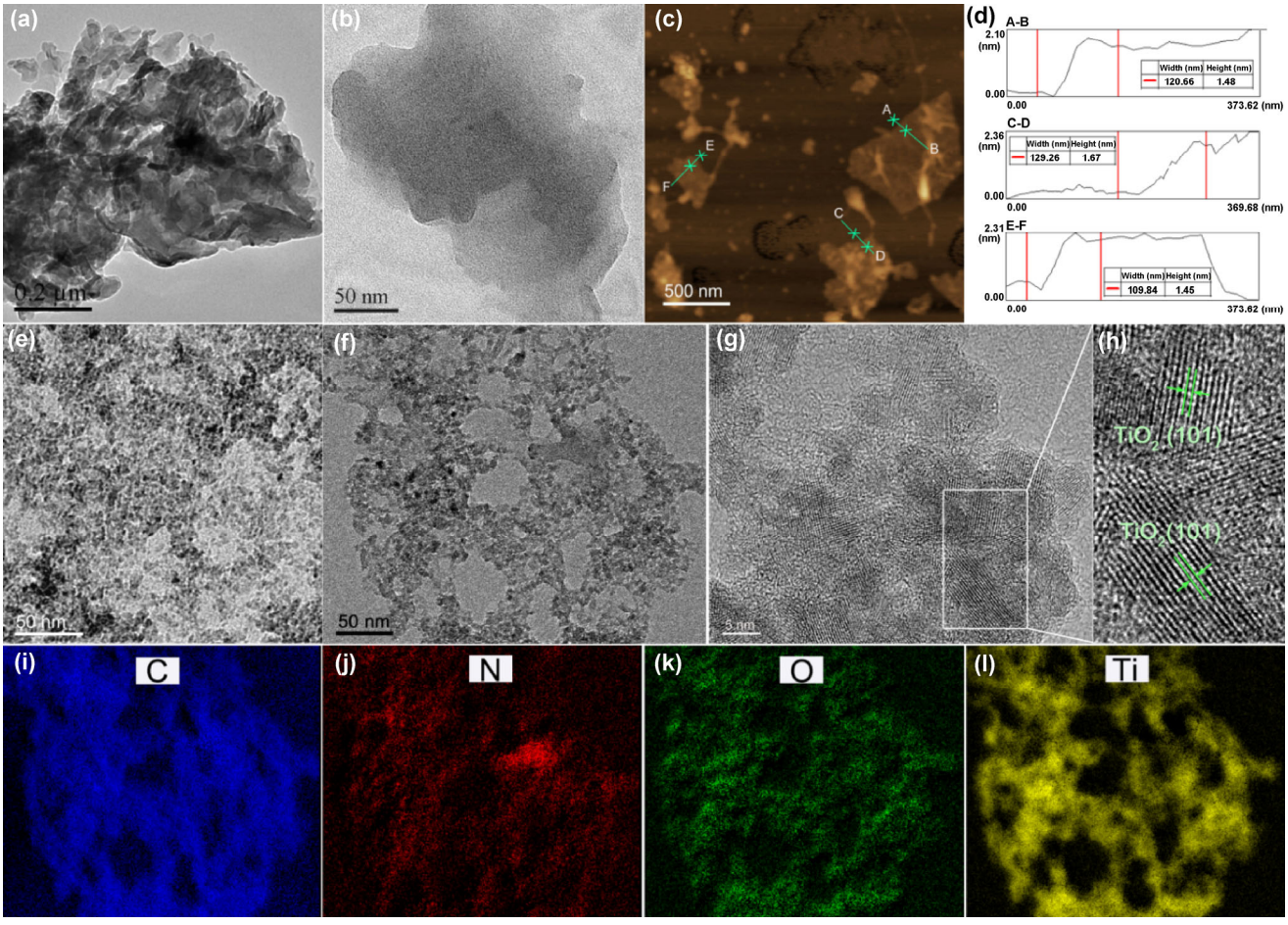

Figure 2 TEM images of (a) bulk CN, and (b) exfoliated CN-NSs hydrosol catalyst. (c) AFM image and (d) corresponding cross-sectional analysis of the CN-NSs hydrosol. (e) TEM image of the TiO_2 hydrosol. (f) TEM and (g) and (h) HRTEM images of the TiO_2/CN-NSs hybrids. (i)–(l) Elemental mapping images.

to the crystallographic spacing of the (101) crystal plane of anatase TiO_2 (Figs. 2(g) and 2(h)) [26, 27]. The elemental mapping images in Figs. 2(i)–2(l) identified the formation of a well-contacted 0D/2D heterostructure with highly dispersed TiO_2/CN-NSs nanojunctions that would facilitate the fast charge carrier transfer during the photocatalytic reaction. In this way, the exfoliated CN-NSs functioned as an ideal 2D substrate, similar to graphene, for supporting metal or metal oxide crystals.

The presence of CN and TiO_2 in the hybrid was also confirmed by the FTIR spectra. The strong characteristic absorption bands of the CN networks were observed in all CN-based materials. This means that the exfoliation and TiO_2 coupling did not alter the typical molecular structure of CN (Fig. 3). The peaks in the region from 1,200 to 1,700 cm^{-1} were attributed to the feature-distinctive stretching modes of tri-s-triazine derivatives, such as trigonal ($N–(C)_3$), from the full condensation, and bridging of C–NH–C from the incomplete condensation [16]. The sharp peak at 810 cm^{-1} belongs to the breathing mode of the tri-s-triazine units. The broad band between 3,000 and 3,600 cm^{-1} belongs to N–H stretches of the terminal amino groups from incomplete condensation [28]. For the pure TiO_2 and TiO_2/CN-NSs hybrid, the broad absorption band at 400–1,000 cm^{-1} corresponds to the Ti–O–Ti stretching vibrations [29]. The additional band between 3,000 and 3,600 cm^{-1} was caused by the adsorbed hydroxyl species on the surface. The FTIR signal of the tri-s-triazine units in the hybrid, marked by a red circle, was overlapped by the strong Ti–O–Ti stretching. The typical absorption bands of CN and TiO_2 skeletons are observable in the hybrid, suggesting the successful synthesis of the TiO_2/CN-NSs composite.

The influence of exfoliation and TiO_2 coupling on the crystal structure of CN materials was examined by XRD, as shown in Fig. S1 (in the Electronic Supplementary Material (ESM)) and Fig. 4. Bulk CN displayed two typical diffraction peaks at 2θ = 12.8° and 27.4°, which were attributed to the (100) in-plane repeating motifs of the tri-s-triazine units, and (002) interlayer stacking of the π-conjugated aromatic system, respectively [30]. When bulk CN was exfoliated into ultrathin NSs, the (100) in-plane diffraction almost disappeared. This can be ascribed to the decreased planar size by the exfoliation process. Meanwhile, a sharp decrease in the diffraction intensity at 27.4° indicated a significant weakening of the interlayer stacking of CN after exfoliation (Fig. S1 in the ESM) [31, 32]. Actually, the (002) diffraction signals of ultrathin CN-NSs with few atomic layers should disappear, or turn to a flat peak, similar to the (002) peak of exfoliated graphene sheets [33, 34]. Hence, it can be deduced that some exfoliated layers are inclined to re-stack into a bulk structure during the water evaporation preparation of the powders [17]. The TiO_2 crystals displayed a pure anatase phase with a crystal size of 5.7 nm, which was calculated by the Scherer's equation, and is consistent with the TEM observations. The diffraction signals of CN and TiO_2 can be observed

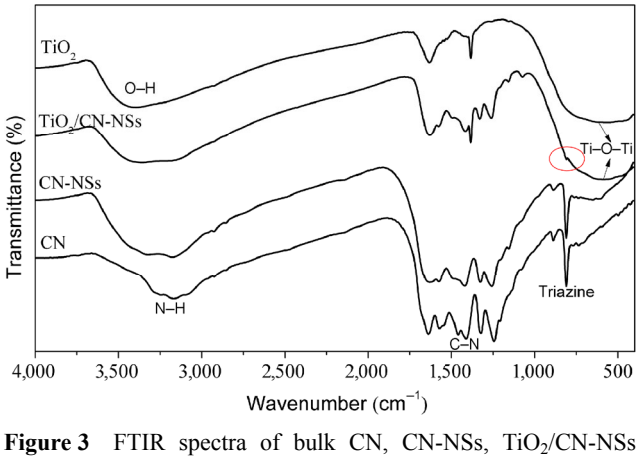

Figure 3 FTIR spectra of bulk CN, CN-NSs, TiO_2/CN-NSs (3:1), and TiO_2.

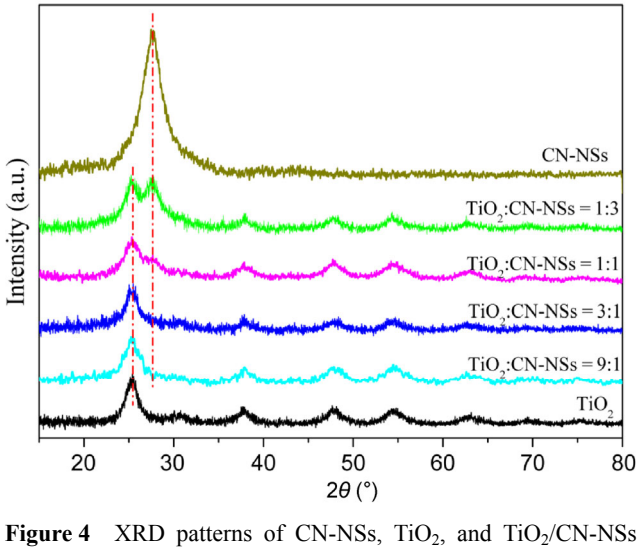

Figure 4 XRD patterns of CN-NSs, TiO_2, and TiO_2/CN-NSs hybrids with different weight ratios.

in the hybrids with low TiO_2 content (TiO_2:CN-NSs = 1:3), indicating their coexistence (Fig. 4). With the increase of TiO_2 content, the diffraction peak at 27.4° became less pronounced, and gradually disappeared. That is to say, when assembling TiO_2 NPs on the surface of CN-NSs, the interfacial contact between them may restrict the re-stacking of the exfoliated CN-NSs layers during their drying to powder-like samples.

To get an insight into the restriction of the layers re-stacking by the embedded TiO_2 NPs, a BET analysis was carried out. Figure 5 displays the nitrogen adsorption–desorption isotherms, and pore-size distributions of the as-prepared samples. The isotherms of all samples were type IV according to the IUPAC classification, indicating the existence of mesopores (Fig. 5(a)) [35]. These mesopores mainly originated from the primary aggregation of crystals. The isotherm profile of CN had the typical H3 hysteresis loops [36], while the profiles of TiO_2 and the hybrids had typical H2 hysteresis loops at the relative pressure (P/P_0 = 0.4–0.8) [37]. This means that the hybrids possessed similar ink-bottle pores as those of the TiO_2 NPs, with a narrow pore-size distribution in the range of about 2–7 nm (Fig. 5(b)). The values of the specific surface area were calculated and compared in Table 1. The TiO_2 NPs possessed a large surface area of 194.6 $m^2 \cdot g^{-1}$ because of their small crystallite size, and good dispersibility. The bulk CN that was prepared by directly heating dicyandiamide had an extremely low surface area of 12.4 $m^2 \cdot g^{-1}$. Although in our previous work we improved the surface area of CN to a value of 87.7 $m^2 \cdot g^{-1}$ by thermal exfoliation [38], herein the surface area of the CN-NSs powders after such liquid-phase exfoliation process decreased to 2.0 $m^2 \cdot g^{-1}$ [39], which is a value much lower than that of other 2D materials like graphene [40]. The result demonstrates that the ultrathin CN layers cannot maintain their 2D morphology and high surface area when they are dried into powders. It seems that the exfoliated fragments re-stacked into a more compressed structure, in contrast to the pristine bulk material, as illustrated in Fig. 1. It should be noted that the surface area of the CN-NSs dramatically increased with the amount of TiO_2 coupling, and then slightly decreased at higher ratios. The hybrids where the ratio of TiO_2 to CN-NSs was 9:1 achieved the largest surface area value of 234.0 $m^2 \cdot g^{-1}$, which is much higher than that of other reported

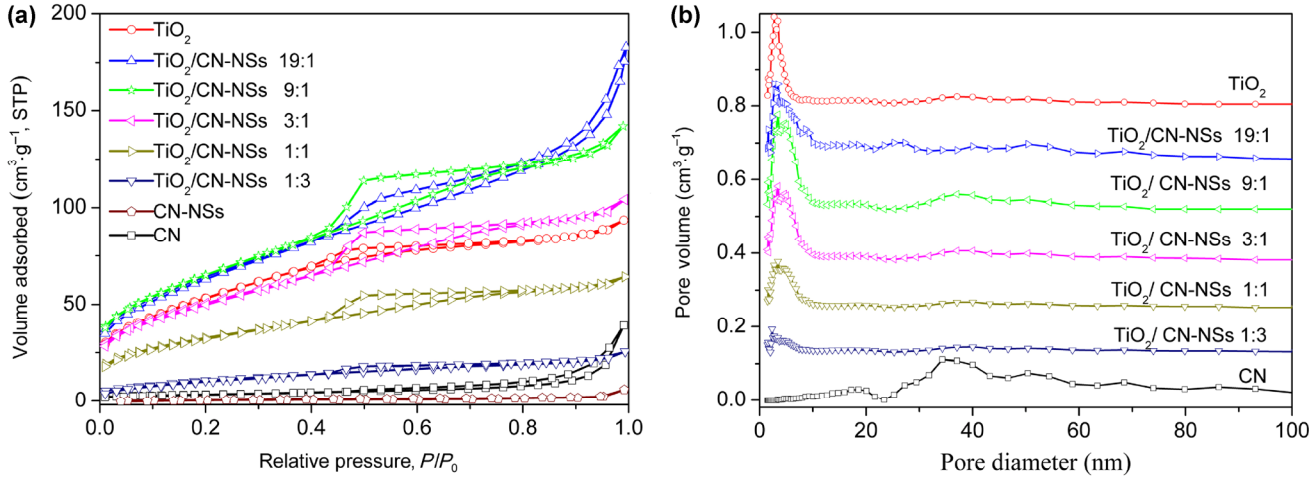

Figure 5 Nitrogen adsorption/desorption isotherms, and pore-size distributions of the as-prepared samples.

Table 1 Specific surface area of CN, CN-NSs, TiO_2, and TiO_2/CN-NSs hybrids with different weight ratios

Samples	CN	CN-NSs	TiO_2	TiO_2/CN-NSs hybrids				
				1:3	1:1	3:1	9:1	19:1
S_{BET}[a] ($m^2 \cdot g^{-1}$)	12.4	2.0	194.6	40.0	116.5	181.7	234.0	223.9

[a]The surface area values were calculated from the N_2 adsorption/ desorption isotherms at 77.3 K using the BET equation.

metal oxide/CN composites [5–9, 20–22]. During their interfacial assembly, the ultrathin CN-NSs were uniformly covered by ultrafine TiO_2 NPs to form strong interactions, instead of existing as isolated ultrathin layers. Therefore, the interfacial interactions between them efficiently hindered the re-stacking of the exfoliated ultrathin CN-NSs layers into a bulk structure, resulting in the significantly enlarged specific surface area.

The XPS technique was introduced to discover the electronic interactions between the CN-NSs and TiO_2 in the hybrid, in additions to the chemical states of the elements. The survey spectra demonstrate that all elements of CN and TiO_2 are present in the hybrid (Fig. S2 in the ESM). The high-resolution XPS spectra of C, N, Ti, and O in the as-obtained samples are compared in Fig. 6. In comparison to bulk CN, no obvious shifts in the binding energy of the C 1s and N 1s core electrons were observed in the CN-NSs, suggesting that the exfoliation did not alter their chemical environments (Figs. 6(a) and 6(b)). The C 1s spectra displayed three peaks at 285.0, 286.4, and 288.5 eV, which were assigned to the adventitious carbon reference for calibration, C–NH– species, and sp^2-hybridized carbon (N–C=N) in the heterocycles, respectively [41, 42]. Interestingly, TiO_2 coupling caused a shift of 0.2 eV towards a higher binding energy for N–C=N (Fig. 6(a)). Such shift verified the strong electronic interaction with TiO_2, leading to a decrease in the electron intensity of the carbon atoms [43, 44]. It is well known that the interaction at the heterojunction interface is favorable for the stability and activity of the catalysts [45]. After curve fitting, the N 1s spectra were divided into three peaks at 399.0, 400.0, and 401.1 eV, corresponding to sp^2-hybridized N (C–N=C) inside triazine rings, bridging N in form of $N–(C)_3$, and N bonded with H (C–N–H), respectively [41, 42]. Similar to C 1s, the N 1s peaks of the hybrid shifted to a higher binding energy (Fig. 6(b)). The Ti 2p spectrum of TiO_2 displayed two distinct peaks at 458.6 and 464.3 eV with a spin-orbital doublet splitting of 5.7 eV, confirming the chemical state of +4 in TiO_2 (Fig. 6(c)) [46]. When supported on the CN-NSs, the higher locations of the Ti 2p peaks in the hybrid were

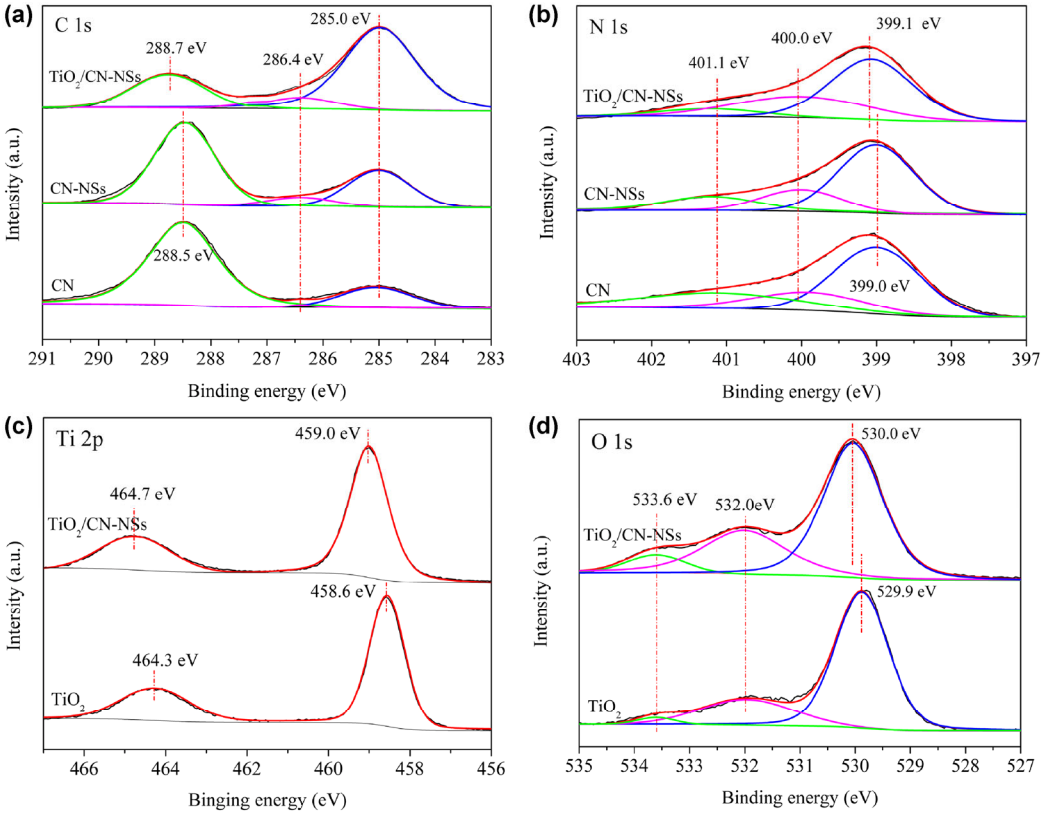

Figure 6 High-resolution XPS of (a) C 1s, (b) N 1s, (c) Ti 2p, and (d) O 1s in bulk CN, CN-NSs, TiO_2, and the TiO_2/CN-NSs hybrid.

also induced by the strong interfacial interactions decreasing the electron intensity of the Ti atom [47]. The absence of Ti–C and Ti–N signals indicated that there were no chemical bonds formed between the CN-NSs and TiO_2 during the assembly [21]. The high-resolution XPS of O 1s is provided in Fig. 6(d). In contrast to pure TiO_2, besides the shift of the Ti–O binding energy to 530.0 eV, the much stronger intensity of O–H at 532.0 eV, and adsorbed O_2 at 533.6 eV, implies that oxygen-containing groups were more readily bounded on the surface of the hybrid. The abundant oxygen-containing groups on the catalyst's surface may facilitate the production of ROS in the system, giving rise to the improvement of the photocatalytic efficiency [48, 49]. Based on the above characterizations, the influence of TiO_2 incorporation on the CN-NSs structure during the synthesis process is schematically illustrated in Fig. 1.

The elemental composition of the samples could not be accurately measured by XPS because the adventitious graphitic carbon was introduced to calibrate the binding energy and the size of the TiO_2 NPs was larger than the detected depth of XPS. TGA was performed to confirm the real content of CN in the hybrid. Upon heating in air, the initial weight loss of 1.7% that occurred between room temperature and 100 ℃ came from the evaporation of surface-bound water (Fig. S3 in the ESM). The following weight loss of 26.2%, which occurred from 100 to 550 ℃, was attributed to the combustion of CN-NSs [8]. Thus, the weight proportion of CN-NSs in the hybrid was determined to be 26.7%, which is close to the theoretical value of 25%.

3.2 Optical, electrochemical, and photoelectrochemical properties

UV–vis DRS was conducted to assess the optical absorption performance of the materials. Pristine CN had an absorption edge at 455 nm (Fig. 7(a)). The bandgap energy was estimated to be 2.80 eV from the converted Tauc plot as a function of photon energy (Fig. 7(b)). Clearly, the exfoliated CN-NSs showed an obvious blue shift of ~25 nm, corresponding to a larger bandgap of 2.97 eV, due to the quantum confinement effect. In contrast to pure TiO_2, the CN-based materials exhibited a strong visible light absorption. The bandgap

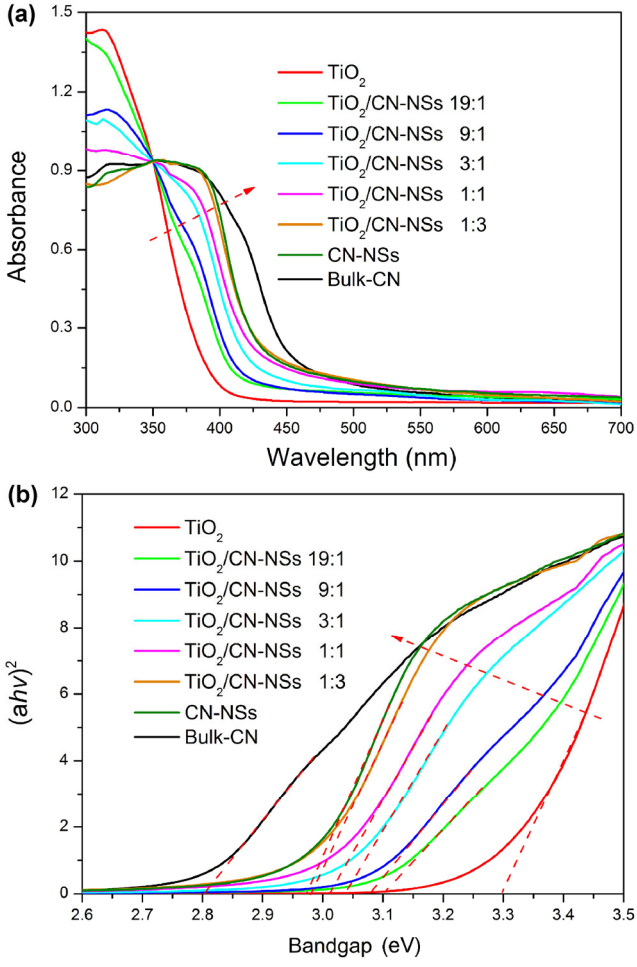

Figure 7 (a) UV–vis DRS of bulk CN, CN-NSs, TiO_2, and TiO_2/CN-NSs hybrid. (b) The converted Tauc plot of $(\alpha h\nu)^2$ versus photon energy ($h\nu$).

energy values of the hybrids fell between those of TiO_2 and the CN-NSs. This can be attributed to the interactions between them [50]. When the content of CN-NSs was increased, the absorption edge stepwise shifted to a longer wavelength, indicating that the introduction of the CN-NSs brought about a wider light absorption. In addition, the hybrid possessed stronger optical absorption intensity within the UV region than CN and the CN-NSs owing to the larger absorption coefficient of TiO_2. Thus different regions in the solar spectrum can be more efficiently absorbed by the TiO_2/CN-NSs hybrid, which favors photocatalysis under solar light. The influence of exfoliation and TiO_2 coupling on the optical properties of CN was studied by the PL spectra (Fig. 8). The emission band of the CN-NSs also displayed a blue shift, as compared with bulk CN [15–17]. It is noticeable that the CN-NSs

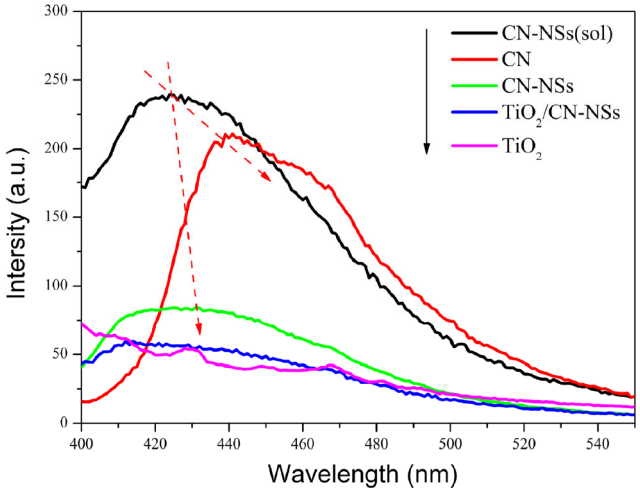

Figure 8 PL spectra of bulk CN, CN-NSs, TiO_2, and the TiO_2/CN-NSs hybrid under a 360 nm excitation. For these measurements, all samples were prepared by dispersing the powders in water to form suspensions, with the exception of the CN-NSs(sol) sample, which was measured directly using hydrosol.

hydrosol (CN-NSs(sol)) exhibited more blue shift and stronger PL emission than the CN-NSs powder. Such difference implies that the acid etching produced more surface defects and drying induced the ultrathin layers to reassemble into a bulk structure with the self-repairing of surface defects. The greatest PL quenching was achieved when TiO_2 NPs assembled on the CN-NSs layers, indicating the reduced recombination loss of photogenerated e^-–h^+ pairs by the efficient charge transfer between them [51].

The improved charge carrier separation of the CN-NSs by the embedded TiO_2 NPs can be further verified by EIS and photocurrent measurements. The diameter of the semicircle at high frequencies in Fig. 9(a) represents the electron-transfer resistance (R_{et}) across the electrode/electrolyte. The Nyquist plot of the CN-NSs(sol) displayed decreased semicircles as compared to CN, indicating that a more efficient charge transfer occurred in the nanosheets than in the bulk material. A similar tendency was obtained in the photocurrent transient response (Fig. 9(b)). Compared with CN, a much stronger photocurrent signal was observed when the TIO electrode was directly coated with the CN-NSs(sol). However, both the conductivity and photocurrent response dramatically decreased in the CN-NSs powders, which again evidenced that the CN-NSs layers reassembled into a bulk structure during their drying. The lowest R_{et} in

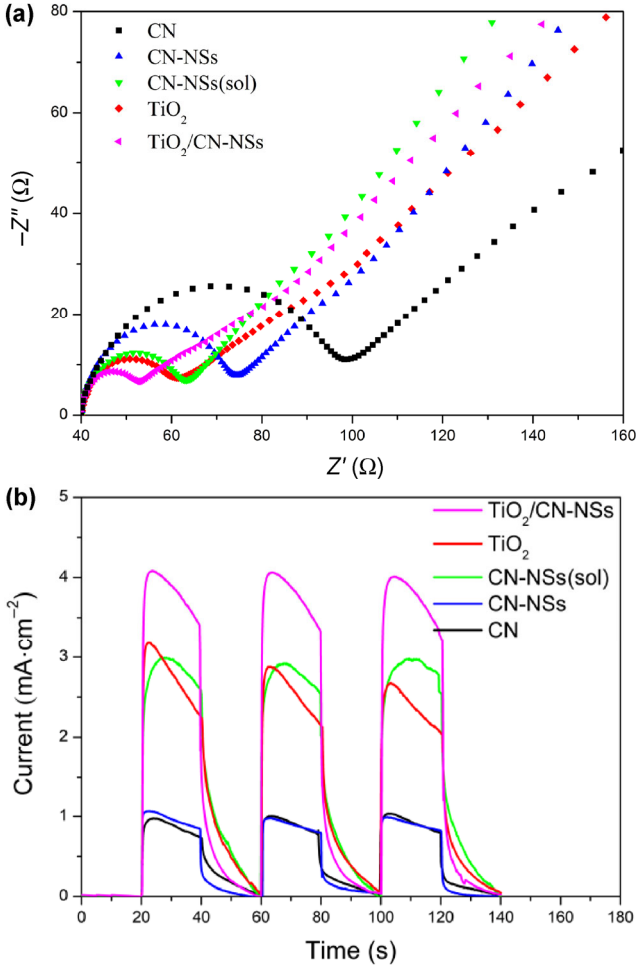

Figure 9 (a) EIS and (b) photocurrent response of bulk CN, CN-NSs, CN-NSs(sol), TiO_2, and the TiO_2/CN-NSs hybrid.

the hybrid suggests that the formation of nanojunctions at the TiO_2/CN-NSs interface effectively reduced the resistance of charge transport. The intensity of the photocurrent in the TiO_2/CN-NSs hybrid was about 4.1 times that in CN, and 1.4 times that in TiO_2. Such dramatic enhancement can be ascribed to the efficient separation of the photogenerated charge carriers between TiO_2 and the CN-NSs.

3.3 Photocatalytic activity and stability

Organic pollutants have widely existed in industrial processes, and have caused a series of serious environmental problems. Herein, RB dye was introduced as a target pollutant to evaluate the photocatalytic activity of the catalysts under simulated solar light irradiation. As shown in Fig. 10(a), the degradation of the RB dye was negligible in the absence of

photocatalyst, indicating that it is a relatively stable structure against direct photolysis. The adsorption capability and concentration of the residual dye molecule (c_0 in Y axis of Fig. 10(a)) were measured after the adsorption–desorption equilibrium. It is well known that a large surface area can provide more possible reactive sites for adsorbing dye molecules. In addition, the aromatic regions of the dye and catalyst are favorable for non-covalent adsorption by π–π stacking [52]. Hence, the hybrid possessed the highest adsorption capacity among all powder catalysts (Fig. S4 in the ESM). The adsorption capacity of the CN-NSs powder catalyst was not as high as that of the sol catalyst, presumably due to the re-stacking of the exfoliated layers during drying. A similar decrease in the photocatalytic activity of the CN-NSs powder catalyst is observed in Fig. 10(a). Although the sol catalyst exhibited a high efficiency for RB degradation, its difficulty in recycling severely restricts its practical application from an economic consideration. Fortunately, the incorporation of TiO_2 NPs brings about a significant enhancement in the photocatalytic efficiency of the CN-NSs powder catalyst under full spectrum irradiation. A similar phenomenon was observed in the photocatalytic reaction under UV, or visible light, irradiation (Fig. S5 in the ESM). The photodegradation curves under the full spectrum irradiation were fitted according to the pseudo-first-order kinetic model, $\ln(c_0/c) = kt$ (Fig. 10(b)).

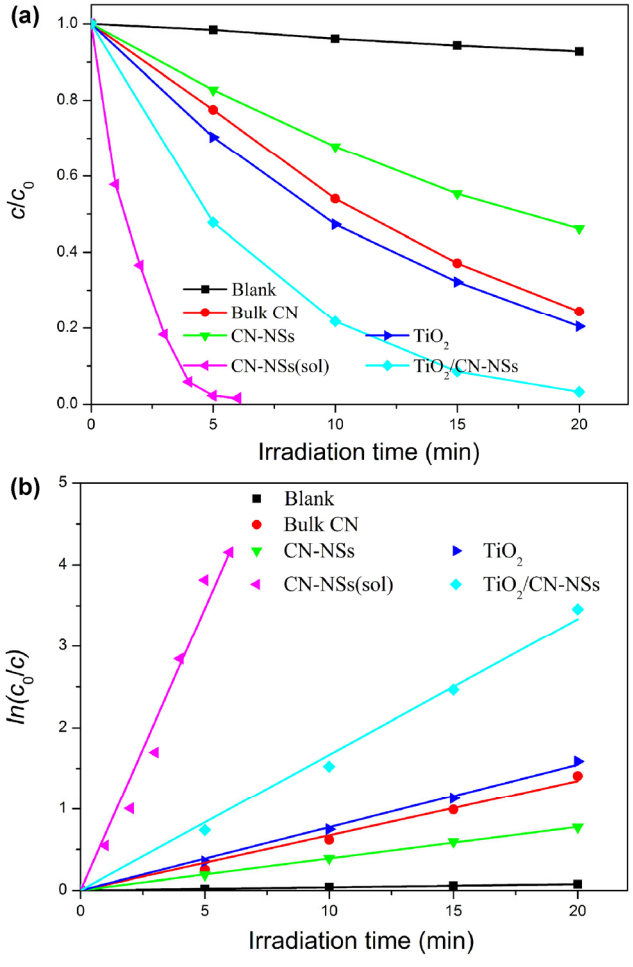

Figure 10 (a) Photocatalytic reaction curves and (b) the corresponding first-order plots of the as-prepared samples for RB degradation under simulated solar light irradiation. The CN-NSs(sol) sample was directly used by keeping the same concentration as the other catalysts.

The rate constant k values were calculated and are given in Table S1 in the ESM. The k of the TiO_2/CN-NSs hybrid was 0.167 min^{-1}, which is a 2.5 and 2.2 folds enhancement over CN and TiO_2, respectively. In the presence of TiO_2, the interaction with the CN layers formed at the interface generated sufficient nanojunctions to hinder the re-stacking of the 2D nanosheets. Thus, the enlarged surface area of the as-obtained hybrid not only allowed access for the dye molecules to the surface, but it also promoted the transfer of the surface carriers across the interface. Combined with the above optical and photoelectrochemical analysis, it can be deduced that the enhancement in photocatalytic performance can be attributed to the enlarged surface area by the well-contacted interface, and the improved charge separation by the well-matched band structure.

Photocatalytic water splitting has been extensively investigated as a promising approach for converting intermittent solar energy to clean and renewable hydrogen fuels. The H_2 production efficiency was evaluated using the Pt-loading samples of CN, CN-NSs(sol), CN-NSs, TiO_2, and TiO_2/CN-NSs (Fig. 11(a)). The loading of Pt NPs on TiO_2 displayed a H_2 production rate of 376.3 μmol·h^{-1}, which is a value close to that of CN (327.7 μmol·h^{-1}), under full spectrum irradiation. The H_2 production activity obviously increased in the exfoliated CN-NSs(sol) system (i.e. loading Pt NPs on the hydrosol materials, and then drying to powders), while it seriously deteriorated in the case of directly loading Pt on the dried powders. The great difference also suggests that the incorporation

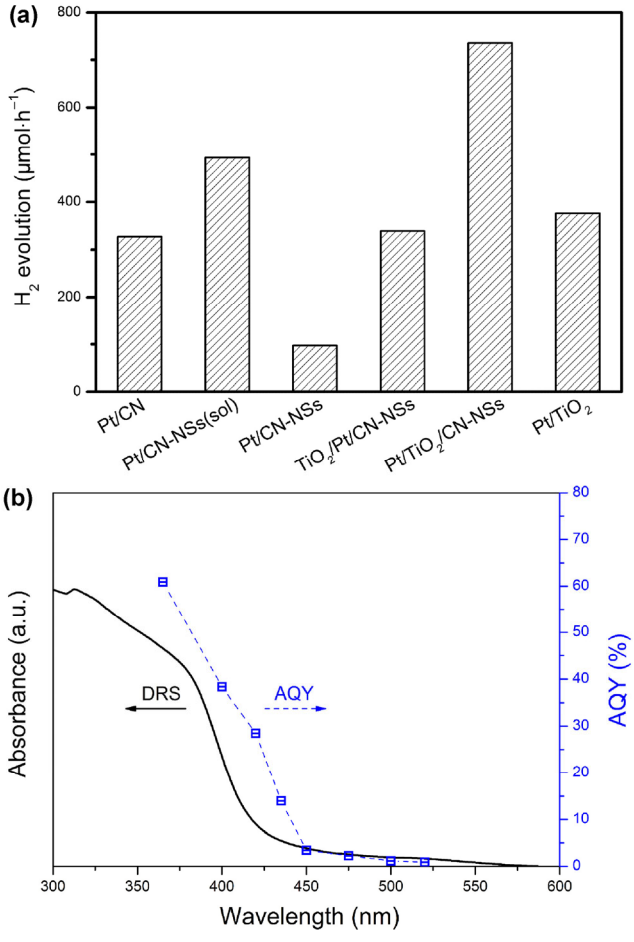

Figure 11 (a) Photocatalytic H_2 production rate for CN, CN-NSs(sol), CN-NSs, TiO_2, and TiO_2/CN-NSs hybrids under full spectrum irradiation. (b) Wavelength-dependent AQY of H_2 production by the TiO_2/CN-NSs hybrid using the corresponding band-pass filters of $\lambda \pm 15$ nm. The UV–vis DRS is overlapped for comparison. Experimental conditions: a 100 mL suspension containing 50 mg of catalyst (0.5 wt.% Pt) and 50 mM AA.

of Pt NPs had some influence on the restriction of interlayer stacking. The TiO_2/CN-NSs hybrid exhibited the highest H_2 production rate of 735.8 μmol·h^{-1} per 50 mg catalyst. The efficiency was much higher than the reported rate by GCN/NT NFs (8,931.3 μmol·g^{-1}·h^{-1}) under simulated solar light [20]. The tendency of the wavelength-dependent AQY curve of the TiO_2/CN-NSs hybrid was similar to its UV–vis DRS (Fig. 11(b)). The hybrid had a high quantum yield of 60.9% at 365 ± 15 nm. Especially under irradiation with visible light at 400 ± 15 nm, the AQY was calculated to be as high as 38.4%. The main reason for such significant improvement may come from the sufficient amount of TiO_2/CN-NSs nanojunctions, which created more electrons transfer channels for charge separation. Further evidence is presented in the controlled experiments regarding the Pt-free photocatalysis, and the location of the Pt loading. Without Pt as co-catalyst, single-component systems such as CN and TiO_2 exhibited extremely low H_2 evolution rates [53]. Interestingly, the hybrid displayed a higher degree of enhancement in comparison to the changes in the Pt loading system (Fig. S6 in the ESM). When the Pt NPs were loaded onto the CN-NSs before coupling with TiO_2, the H_2 production rate become much lower, which indicated that the incorporation of Pt blocked the electron transfer channels between TiO_2 and CN-NSs. Moreover, the influence of the loading order of Pt NPs implies that the active sites for H_2 production were on the TiO_2 NPs instead of the CN-NSs. That is to say, the H_2 molecules were most likely to be produced by the electrons on the conduction band (CB) of the TiO_2 NPs that were directly generated within TiO_2, or transferred from the CB of CN-NSs.

Since the interaction at TiO_2/CN-NSs interface contributes a lot to the improved photocatalytic performance, the efficiency may be dependent on the incorporation ratio of TiO_2 to CN-NSs. The photoactivity of the hybrid increases with the TiO_2 content at first and then decreases when the weight ratio of TiO_2 to CN-NSs is higher than 3:1 (Fig. S7 in the ESM). The consistent results are obtained from both RB degradation and H_2 production. Based on the above analysis, the hybrid at the ratio of 9:1 possesses the largest surface area, while the pristine CN can harness the photons in the widest light region. However, the best photocatalytic performance is achieved in the hybrid with a weight ratio of TiO_2 to CN-NSs as 3:1. This suggests that an appropriate balance between absorbing enough photons for charge generation and producing sufficient nanojunctions for charge separation is reached at this optimal ratio.

Besides the activity, the stability of the photocatalysts is crucial for composite structure because of the possible leakage of one component from another. Figure 12 displays the cyclic activity of TiO_2/CN-NSs hybrid photocatalyst within several consecutive runs. There is no significant loss in photocatalytic activity after each cycle, suggesting that the strong interfacial

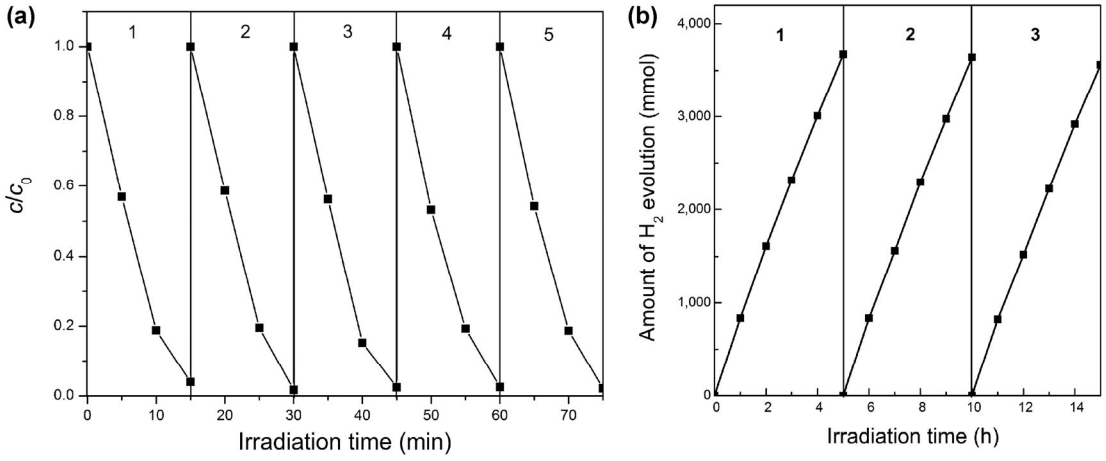

Figure 12 (a) Cycle photocatalytic behaviors towards RB degradation, and H_2 production using the TiO_2/CN-NSs hybrid under full spectrum irradiation.

interaction between TiO_2 and CN-NSs benefits the stable heterostructure. As further evidence, the analysis of XRD, FTIR, and TEM of the fresh and used hybrid photocatalyst are compared in Figs. S8–S10 in the ESM. No obvious difference in absorption bands demonstrates the stable chemical structure throughout the whole reaction.

3.4 Photocatalytic mechanism of TiO_2/CN-NSs heterostructure

A lively discussion on the synergetic effect between CN and TiO_2 has appeared in the literature. For instance, several groups reported a Z-scheme mechanism under UV light. In their system, the photoinduced e^- transferred from the CB of TiO_2 to the valence band (VB) of CN, while the e^- and h^+ were kept in the CB of CN, and VB of TiO_2, respectively [8, 9, 54]. On the other hand, there are some reports that illustrate a different charge transport pathway, i.e. the photoinduced e^- transferring from CN(CB) to TiO_2(CB), and the h^+ transferring from TiO_2(VB) to CN(VB) [10, 20, 22]. To reveal the photocatalytic mechanism of the TiO_2/CN-NSs hybrid from this synthetic system, trapping experiments were conducted by adding individual scavengers to the photocatalytic reaction. The scavengers used were t-BuOH for $^{\cdot}OH$, BQ for $O_2^{-\cdot}$, and EDTA-2Na for h^+ (Fig. 13). The degradation rate decreased slightly with the addition of t-BuOH, revealing the least contribution of $^{\cdot}OH$ in the TiO_2/CN-NSs hybrid. The addition of EDTA-2Na caused an obvious interference with the RB degradation. Moreover, the photocatalytic reaction was remarkably inhibited in the absence of BQ. From this it can be concluded that h^+ and $O_2^{-\cdot}$ were the main active species, with an order of $O_2^{-\cdot}$ > h^+, during the photodegradation process. Generally, the $O_2^{-\cdot}$ species originated from the reduction of the dissolved O_2 by the photoinduced e^- [55]. The $^{\cdot}OH$ radicals were produced by the oxidation of adsorbed OH^-. Because CN(VB) had a more negative potential than $^{\cdot}OH/OH^-$, only the photogenerated h^+ in TiO_2(VB) were capable of oxidizing the adsorbed OH^- into $^{\cdot}OH$, according to their potential locations. Therefore, the identification of weak contributions of $^{\cdot}OH$ radicals explains the location of holes on CN(VB).

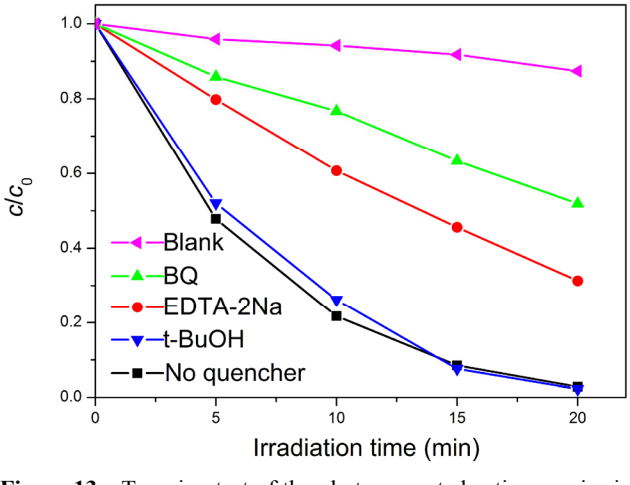

Figure 13 Trapping test of the photogenerated active species in the TiO_2/CN-NSs hybrid.

For comparison, the results of the trapping experiments over CN and TiO_2 catalysts were presented in Fig. S11 in the ESM. The $O_2^{\cdot-}$ generated by CN had a major contribution toward the degradation of RB, whereas the h^+ occurring in the TiO_2 system was more responsible than $O_2^{\cdot-}$ and $^{\cdot}OH$ for the reaction. The difference of the main active species between CN and TiO_2 may arise from the much weaker oxidation ability of CN(VB), in comparison with TiO_2(VB) [21]. It is noted that the photocatalytic efficiency of CN displayed a great improvement with the addition of EDTA-2Na, suggesting that the capture of h^+ reduced the recombination loss of the photoinduced e^-. Although the content of TiO_2 (73.3% from TGA result) was dominant in the hybrid, the contributions of the active species are inconsistent with pure TiO_2. The lesser contributions of h^+ and $^{\cdot}OH$ in the hybrid photocatalyst also suggest the immigration of h^+ from TiO_2(VB) to the CN-NSs(VB) at the junctions. Combined with the results of the Pt location for H_2 production, it is convincible to propose the following charge transfer pathway in the hybrid system (Fig. 14). Both the CN-NSs and TiO_2 can absorb the simulated solar light to produce charge carriers. Owing to the matched band structure, the photogenerated e^- of CN-NSs(CB) readily transferred to the TiO_2(CB), while the h^+ migrated from the TiO_2(VB) to the CN-NSs(VB). Thus the recombination of the photogenerated e^-–h^+ pairs was sufficiently reduced, leaving more e^- in the TiO_2(CB) to react with the dissolved O_2, and more h^+ in the CN-NSs(VB) to directly oxidize the dye molecules. Apparently, the RB degradation depends more on the former reaction because of the relative weak oxidization ability of CN-NSs(VB). In the case of water splitting, the transferred e^- was collected by the Pt NPs on the TiO_2 to produce H_2 molecules.

4 Conclusions

In summary, we have developed a direct interfacial assembly strategy for the construction of TiO_2 heterostructures modified with CN-NSs. First, TiO_2 NPs of a size of 4–8 nm were uniformly dispersed on the surface of the CN-NSs. In contrast to the serious re-stacking in the single-component CN-NSs system, the strong interaction with TiO_2 effectively hindered the re-stacking of the 2D nanosheets when the samples were dried to powders for the heterogeneous photocatalysis. Consequently, and as far as we know, among the reported metal oxide/CN composites, the TiO_2/CN-NSs hybrid with a controlled ratio possesses the highest specific surface area with a value of 234.0 $m^2 \cdot g^{-1}$. The evaluation of the photocatalytic activity indicates that the composite with the optimal ratio of TiO_2 to CN-NSs of 3:1 showed a remarkably enhanced performance due to the enlarged surface area and improved charge separation. The rate constant k for the RB degradation was calculated to be 0.167 min^{-1}, which is a 2.5 and 2.2 folds enhancement over CN and TiO_2, respectively. The H_2 production rate was as high as 735.8 $\mu mol \cdot h^{-1}$ per 50 mg catalyst. The hybrid yielded an impressive AQY value of 38.4% at 400 ± 15 nm. The composite structure displayed a good stability with no obvious deactivation during the cyclic photocatalytic reactions. Furthermore, a possible mechanism of the TiO_2/CN-NSs hybrid from this

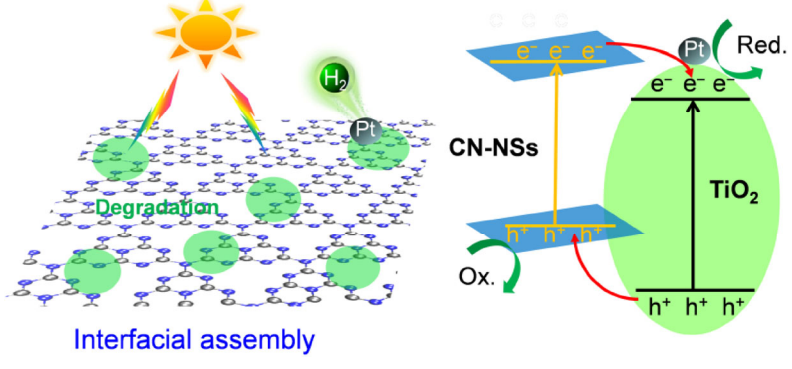

Figure 14 The structure and possible photocatalytic mechanism of a TiO_2/CN-NSs hybrid as a bifunctional catalyst for dye degradation and H_2 production.

synthetic system was proposed based on the trapping test and Pt loading order. The h^+ and $O_2^{-\cdot}$ were the main active species, with an order of $O_2^{-\cdot} > h^+$, for the RB degradation. The production of H_2 molecules most likely occurred on the surface of TiO_2. Overall, this work not only provides a facile approach for constructing semiconductor/CN-NSs heterostructures with a well-contacted interface, but it also highlights the superiority of CN-NSs as a promising substrate for diverse applications.

Acknowledgements

We thank the Analysis and Testing Center, Huazhong University of Science and Technology for their assistance in characterization of materials. This work is supported by the National Natural Science Foundation of China (No. 21571071), Hubei Provincial Natural Science Foundation of China (No. 2015CFB313), and the Fundamental Research Funds for the Central Universities (No. 2015QN183).

Electronic Supplementary Material: Supplementary material (XRD patterns, XPS survey spectra, TGA curve, adsorption capacity comparison, photocatalytic activity for TiO_2/CN-NSs hybrid with different weight ratio, FTIR spectra of the cycled photocatalyst, trapping test, and a list of degradation rate constants) is available in the online version of this article at http://dx.doi.org/10.1007/s12274-017-1453-2.

References

[1] Asahi, R.; Morikawa, T.; Irie, H.; Ohwaki, T. Nitrogen-doped titanium dioxide as visible-light-sensitive photocatalyst: Designs, developments, and prospects. *Chem. Rev*. **2014**, *114*, 9824–9852.

[2] Lang, X. J.; Ma, W. H.; Chen, C. C.; Ji, H. W.; Zhao, J. C. Selective aerobic oxidation mediated by TiO_2 photocatalysis. *Acc. Chem. Res*. **2014**, *47*, 355–363.

[3] Ma, Y.; Wang, X. L.; Jia, Y. S.; Chen, X. B.; Han, H. X.; Li, C. Titanium dioxide-based nanomaterials for photocatalytic fuel generations. *Chem. Rev*. **2014**, *114*, 9987–10043.

[4] Zhao, D.; Yang, C. F. Recent advances in the TiO_2/CdS nanocomposite used for photocatalytic hydrogen production and quantum-dot-sensitized solar cells. *Renew. Sust. Energ. Rev*. **2016**, *54*, 1048–1059.

[5] Hao, R. R.; Wang, G. H.; Tang, H.; Sun, L. L.; Xu, C.; Han, D. Y. Template-free preparation of macro/mesoporous g-C_3N_4/TiO_2 heterojunction photocatalysts with enhanced visible light photocatalytic activity. *Appl. Catal. B: Environ*. **2016**, *187*, 47–58.

[6] Jiang, Z. F.; Zhu, C. Z.; Wan, W. M.; Qian, K.; Xie, J. M. Constructing graphite-like carbon nitride modified hierarchical yolk–shell TiO_2 spheres for water pollution treatment and hydrogen production. *J. Mater. Chem. A* **2016**, *4*, 1806–1818.

[7] Sridharan, K.; Jang, E. Y.; Park, T. J. Novel visible light active graphitic C_3N_4–TiO_2 composite photocatalyst: Synergistic synthesis, growth and photocatalytic treatment of hazardous pollutants. *Appl. Catal. B: Environ*. **2013**, *142–143*, 718–728.

[8] Yu, J. G.; Wang, S. H.; Low, J. X.; Xiao, W. Enhanced photocatalytic performance of direct Z-scheme g-C_3N_4–TiO_2 photocatalysts for the decomposition of formaldehyde in air. *Phys. Chem. Chem. Phys*. **2013**, *15*, 16883–16890.

[9] Muñoz-Batista, M. J.; Kubacka, A.; Fernández-García, G. Effect of g-C_3N_4 loading on TiO_2-based photocatalysts: UV and visible degradation of toluene. *Catal. Sci. Technol*. **2014**, *4*, 2006–2015.

[10] Gu, L.; Wang, J. Y.; Zou, Z. J.; Han, X. J. Graphitic-C_3N_4-hybridized TiO_2 nanosheets with reactive {001} facets to enhance the UV- and visible-light photocatalytic activity. *J. Hazard. Mater*. **2014**, *268*, 216–223.

[11] Guo, S. E.; Deng, Z. P.; Li, M. X.; Jiang, B. J.; Tian, C. G.; Pan, Q. J.; Fu, H. G. Phosphorus-doped carbon nitride tubes with a layered micro-nanostructure for enhanced visible-light photocatalytic hydrogen evolution. *Angew. Chem., Int. Ed*. **2016**, *55*, 1830–1834.

[12] Han, Q.; Zhao, F.; Hu, C. G.; Lv, L. X.; Zhang, Z. P.; Chen, N.; Qu, L. T. Facile production of ultrathin graphitic carbon nitride nanoplatelets for efficient visible-light water splitting. *Nano Res*. **2015**, *8*, 1718–1728.

[13] Mao, J.; Peng, T. Y.; Zhang, X. H.; Li, K.; Ye, L. Q.; Zan, L. Effect of graphitic carbon nitride microstructures on the activity and selectivity of photocatalytic CO_2 reduction under visible light. *Catal. Sci. Technol*. **2013**, *3*, 1253–1260.

[14] Xu, L.; Huang, W. Q.; Wang, L. L.; Tian, Z. A.; Hu, W. Y.; Ma, Y. M.; Wang, X.; Pan, A. L.; Huang, G. F. Insights into enhanced visible-light photocatalytic hydrogen evolution of g-C_3N_4 and highly reduced graphene oxide composite: The role of oxygen. *Chem. Mater*. **2015**, *27*, 1612–1621.

[15] Zhang, X. D.; Xie, X.; Wang, H.; Zhang, J. J.; Pan, B. C.; Xie, Y. Enhanced photoresponsive ultrathin graphitic-phase C_3N_4 nanosheets for bioimaging. *J. Am. Chem. Soc*. **2013**, *135*, 18–21.

[16] Ma, T. Y.; Tang, Y. H.; Dai, S.; Qiao, S. Z. Proton-functionalized two-dimensional graphitic carbon nitride nanosheet: An excellent metal-/label-free biosensing platform. *Small* **2014**, *10*, 2382–2389.

[17] Xu, J.; Zhang, L. W.; Shi, R.; Zhu, Y. F. Chemical exfoliation of graphitic carbon nitride for efficient heterogeneous photocatalysis. *J. Mater. Chem. A* **2013**, *1*, 14766–14772.

[18] Schwinghammer, K.; Mesch, M. B.; Duppel, V.; Ziegler, C.; Senker, J.; Lotsch, B. V. Crystalline carbon nitride nanosheets for improved visible-light hydrogen evolution. *J. Am. Chem. Soc*. **2014**, *136*, 1730–1733.

[19] Cheng, F. X.; Wang, H. N.; Dong, X. P. The amphoteric properties of g-C_3N_4 nanosheets and fabrication of their relevant heterostructure photocatalysts by an electrostatic re-assembly route. *Chem. Commun*. **2015**, *51*, 7176–7179.

[20] Han, C.; Wang, Y. D.; Lei, Y. P.; Wang, B.; Wu, N.; Shi, Q.; Li, Q. *In situ* synthesis of graphitic-C_3N_4 nanosheet hybridized N-doped TiO_2 nanofibers for efficient photocatalytic H_2 production and degradation. *Nano Res*. **2015**, *8*, 1199–1209.

[21] Li, Y. L.; Wang, J. S.; Yang, Y. L.; Zhang, Y.; He, D.; An, Q. E.; Cao, G. Z. Seed-induced growing various TiO_2 nanostructures on g-C_3N_4 nanosheets with much enhanced photocatalytic activity under visible light. *J. Hazard. Mater*. **2015**, *292*, 79–89.

[22] Tong, Z. W.; Yang, D.; Xiao, T. X.; Tian, Y.; Jiang, Z. Y. Biomimetic fabrication of g-C_3N_4/TiO_2 nanosheets with enhanced photocatalytic activity toward organic pollutant degradation. *Chem. Eng. J*. **2015**, *260*, 117–125.

[23] Paek, S. M.; Jung, H.; Park, M.; Lee, J. K.; Choy, J. H. An inorganic nanohybrid with high specific surface area: TiO_2-pillared MoS_2. *Chem. Mater*. **2005**, *17*, 3492–3498.

[24] Qiu, B. C.; Li, Q. Y.; Shen, B.; Xing, M. Y.; Zhang, J. L. Stöber-like method to synthesize ultradispersed Fe_3O_4 nanoparticles on graphene with excellent photo-Fenton reaction and high-performance lithium storage. *Appl. Catal. B: Environ*. **2016**, *183*, 216–223.

[25] Su, D.; Wang, J. Y.; Tang, Y. P.; Liu, C.; Liu, L. F.; Han, X. J. Constructing WO_3/TiO_2 composite structure towards sufficient use of solar energy. *Chem. Commun*. **2011**, *47*, 4231–4233.

[26] Wang, J. Y.; Zhao, Y. Z.; Xu, X. C.; Feng, X. L.; Yu, J. X.; Li, T. A facile interfacial assembling strategy for synthesizing yellow TiO_2 flakes with a narrowed bandgap. *RSC Adv*. **2015**, *5*, 58176–58183.

[27] Wang, J. Y.; Han, X. J.; Liu, C.; Zhang, W.; Cai, R. X.; Liu, Z. H. Adjusting the crystal phase and morphology of titania via a soft chemical process. *Cryst. Growth Des*. **2010**, *10*, 2185–2191.

[28] Ong, W. J.; Tan, L. L.; Chai, S. P.; Yong, S. T.; Mohamed, A. R. Surface charge modification via protonation of graphitic carbon nitride (g-C_3N_4) for electrostatic self-assembly construction of 2D/2D reduced graphene oxide (rGO)/g-C_3N_4 nanostructures toward enhanced photocatalytic reduction of carbon dioxide to methane. *Nano Energy* **2015**, *13*, 757–770.

[29] Gu, L. A.; Wang, J. Y.; Cheng, H.; Zhao, Y. Z.; Liu, L. F.; Han, X. J One-step preparation of graphene-supported anatase TiO_2 with exposed {001} facets and mechanism of enhanced photocatalytic properties. *ACS Appl. Mater. Interfaces* **2013**, *5*, 3085–3093.

[30] Liang, Q. H.; Li, Z.; Yu, X. L.; Huang, Z. H.; Kang, F. Y.; Yang, Q. H. Macroscopic 3D porous graphitic carbon nitride monolith for enhanced photocatalytic hydrogen evolution. *Adv. Mater*. **2015**, *27*, 4634–4639.

[31] Tian, J. Q.; Liu, Q.; Asiri, A. M.; Al-Youbi, A. O.; Sun, X. P. Ultrathin graphitic carbon nitride nanosheet: A highly efficient fluorosensor for rapid, ultrasensitive detection of Cu^{2+}. *Anal. Chem*. **2013**, *85*, 5595–5599.

[32] Yang, S. B.; Gong, Y. J.; Zhang, J. S.; Zhan, L.; Ma, L. L.; Fang, Z. Y.; Vajtai, R.; Wang, X. C.; Ajayan, P. M. Exfoliated graphitic carbon nitride nanosheets as efficient catalysts for hydrogen evolution under visible light. *Adv. Mater*. **2013**, *25*, 2452–2456.

[33] Feng, H. B.; Wu, Y. M.; Li, J. H. Direct exfoliation of graphite to graphene by a facile chemical approach. *Small* **2014**, *10*, 2233–2238.

[34] Feng, H. B.; Cheng, R.; Zhao, X.; Duan, X. F.; Li, J. H. A low-temperature method to produce highly reduced graphene oxide. *Nat. Commun*. **2013**, *4*, 1539.

[35] Sing, K. S. W.; Everett, D. H.; Haul, R. A. W.; Moscou, L.; Pierotti, R. A.; Rouquerol, J.; Siemieniewska, T. Physical and biophysical chemistry division commission on colloid and surface chemistry including catalysis. *Pure Appl. Chem*. **1985**, *57*, 603–619.

[36] Zhang, J. Y.; Wang, Y. H.; Jin, J.; Zhang, J.; Lin, Z.; Huang, F.; Yu, J. G. Efficient visible-light photocatalytic hydrogen evolution and enhanced photostability of core/shell CdS/g-C_3N_4 nanowires. *ACS Appl. Mater. Interfaces* **2013**, *5*, 10317–10324.

[37] Nguyen, P. T. M.; Fan, C. Y.; Do, D. D.; Nicholson, D. On the cavitation-like pore blocking in ink-bottle pore: Evolution of hysteresis loop with neck size. *J. Phys. Chem. C* **2013**, *117*, 5475–5484.

[38] Pandiselvi, K.; Fang, H. F.; Huang, X. B.; Wang, J. Y.; Xu, X. C.; Li, T. Constructing a novel carbon nitride/polyaniline/ZnO ternary heterostructure with enhanced photocatalytic performance using exfoliated carbon nitride nanosheets as supports. *J. Hazard. Mater*. **2016**, *314*, 67–77.

[39] Zhang, Z. Y.; Liu, K. C.; Feng, Z. Q.; Bao, Y. N.; Dong, B. Hierarchical sheet-on-sheet $ZnIn_2S_4$/g-C_3N_4 heterostructure with highly efficient photocatalytic H_2 production based on photoinduced interfacial charge transfer. *Sci. Rep*. **2016**, *6*, 19221.

[40] Castarlenas, S.; Rubio, C.; Mayoral, Á.; Téllez, C.; Coronas, J. Few-layer graphene by assisted-exfoliation of graphite with layered silicate. *Carbon* **2014**, *73*, 99–105.

[41] He, F.; Chen, G.; Yu, Y. G.; Hao, S.; Zhou, Y. S.; Zheng, Y. Facile approach to synthesize g-PAN/g-C_3N_4 composites with enhanced photocatalytic H_2 evolution activity. *ACS Appl. Mater. Interfaces* **2014**, *6*, 7171–7179.

[42] Li, J. H.; Shen, B.; Hong, Z. H.; Lin, B. Z.; Gao, B. F.; Chen, Y. L. A facile approach to synthesize novel oxygen-doped g-C_3N_4 with superior visible-light photoreactivity. *Chem. Commun*. **2012**, *48*, 12017–12019.

[43] Lin, L.; Li, M.; Jiang, L. Q.; Li, Y. F.; Liu, D. J.; He, X. Q.; Cui, L. L. A novel iron (II) polyphthalocyanine catalyst assembled on graphene with significantly enhanced performance for oxygen reduction reaction in alkaline medium. *J. Power Sources* **2014**, *268*, 269–278.

[44] Jiang, Y. Y.; Lu, Y. Z.; Lv, X. Y.; Han, D. X.; Zhang, Q. X.; Niu, L.; Chen, W. Enhanced catalytic performance of Pt-free iron phthalocyanine by graphene support for efficient oxygen reduction reaction. *ACS Catal*. **2013**, *3*, 1263–1271.

[45] Jiang, Z. Z.; Wang, Z. B.; Chu, Y. Y.; Gu, D. M.; Yin, G. P. Ultrahigh stable carbon riveted Pt/TiO_2–C catalyst prepared by *in situ* carbonized glucose for proton exchange membrane fuel cell. *Energy Environ. Sci*. **2011**, *4*, 728–735.

[46] Wagner, C. D.; Riggs, W. M.; Davis, L. E.; Moulder, J. F.; Mullenberg, G. E. *Handbook of X-ray Photoelectron Spectroscopy*; Perkin-Elmer Corporation: Minnesota, 1979; pp 68–69.

[47] Cheng, H.; Feng, X. L.; Wang, D. L.; Xu, M.; Pandiselvi, K.; Wang, J. Y.; Zou, Z. J.; Li, T. Synthesis of highly stable and methanol-tolerant electrocatalyst for oxygen reduction: Co supporting on N-doped-C hybridized TiO_2. *Electrochim. Acta* **2015**, *180*, 564–573.

[48] Wang, J. Y.; Liu, Z. H.; Cai, R. X. A new role for Fe^{3+} in TiO_2 hydrosol: Accelerated photodegradation of dyes under visible light. *Environ. Sci. Technol*. **2008**, *42*, 5759–5764.

[49] Tran, T. H.; Nosaka, A. Y.; Nosaka, Y. Adsorption and photocatalytic decomposition of amino acids in TiO_2 photocatalytic systems. *J. Phys. Chem. B* **2006**, *110*, 25525–25531.

[50] Liu, H.; Jin, Z. T.; Xu, Z. Z. Hybridization of $Cd_{0.2}Zn_{0.8}S$ with g-C_3N_4 nanosheets: A visible-light-driven photocatalyst for H_2 evolution from water and degradation of organic pollutants. *Dalton Trans*. **2015**, *44*, 14368–14375.

[51] Hu, J. H.; Wang, L. J.; Zhang, P.; Liang, C. H.; Shao, G. S. Construction of solid-state Z-scheme carbon-modified TiO_2/WO_3 nanofibers with enhanced photocatalytic hydrogen production. *J. Power Sources* **2016**, *328*, 28–36.

[52] Zhang, H.; Lv, X. J.; Li, Y. M.; Wang, Y.; Li, J. H. P25-graphene composite as a high performance photocatalyst. *ACS Nano* **2010**, *4*, 380–386.

[53] Jiang, X. L; Fu, X. L; Zhang, L.; Meng, S. G.; Chen, S. F. Photocatalytic reforming of glycerol for H_2 evolution on Pt/TiO_2: Fundamental understanding the effect of co-catalyst Pt and the Pt deposition route. *J. Mater. Chem. A* **2015**, *3*, 2271–2282.

[54] Huang, Z. A.; Sun, Q.; Lv, K. L.; Zhang, Z. H.; Li, M.; Li, B. Effect of contact interface between TiO_2 and g-C_3N_4 on the photoreactivity of g-C_3N_4/TiO_2 photocatalyst: (001) vs. (101) facets of TiO_2. *Appl. Catal. B: Environ*. **2015**, *164*, 420–427.

[55] Zhang, H.; Guo, L. H.; Zhao, L. X.; Wan, B.; Yang, Y. Switching oxygen reduction pathway by exfoliating graphitic carbon nitride for enhanced photocatalytic phenol degradation. *J. Phys. Chem. Lett*. **2015**, *6*, 958–963.